The Redshift and Star Formation Mode of AzTEC2: A Pair of Massive Galaxies at z = 4.63

Jiménez-Andrade, E. F.; Zavala, J. A.; Magnelli, B.; Casey, C. M.; Liu, D.; Romano- Díaz, E.; Schinnerer, E.; Harrington, K.; Aretxaga, I.; Karim, A.; ...

The Astrophysical Journal, 890:171 (12pp), 2020 February 20 https://doi.org/10.3847/1538-4357/ab6dec

The Redshift and Star Formation Mode of AzTEC2: A Pair of Massive Galaxies at $z = 4.63$

E. F. Jiménez-Andrade[1,2], J. A. Zavala[3], B. Magnelli[2], C. M. Casey[3], D. Liu[4], E. Romano-Díaz[2], E. Schinnerer[4], K. Harrington[2], I. Aretxaga[5], A. Karim[2], J. Staguhn[6,7], A. D. Burnham[3], A. Montaña[8], V. Smolčić[9], M. Yun[10], F. Bertoldi[2], and D. Hughes[5]

[1] National Radio Astronomy Observatory, 520 Edgemont Road, Charlottesville, VA 22903, USA; ejimenez@nrao.edu
[2] Argelander Institute for Astronomy, University of Bonn, Auf dem Hügel 71, D-53121 Bonn, Germany
[3] Department of Astronomy, The University of Texas at Austin, 2515 Speedway Blvd Stop C1400, Austin, TX 78712, USA
[4] Max Planck Institut für Astronomie, Königstuhl 17, D-69117, Heidelberg, Germany
[5] Instituto Nacional de Astrofísica, Óptica y Electrónica (INAOE), Luis Enrique Erro 1, Sta. Ma. Tonantzintla, Puebla, MÉxico
[6] The Henry A. Rowland Department of Physics and Astronomy, Johns Hopkins University, 3400 North Charles Street, Baltimore, MD 21218, USA
[7] Observational Cosmology Lab, Code 665, NASA Goddard Space Flight Center, Greenbelt, MD 20771, USA
[8] CONACyT - Instituto Nacional de Astrofísica, Óptica y Electrónica, Luis E. Erro 1, Tonantzintla, Puebla, MÉxico
[9] Faculty of Science, University of Zagreb, Bijenička c. 32, 10002 Zagreb, Croatia
[10] Department of Astronomy, University of Massachusetts, Amherst, MA 01003, USA

Received 2019 October 28; revised 2020 January 10; accepted 2020 January 16; published 2020 February 26

Abstract

We combine observations from the Atacama Large Millimeter/submillimeter Array and the NOrthern Extended Millimeter Array to assess the redshift and to study the star formation conditions in AzTEC2, one of the brightest submillimeter galaxies (SMGs) in the COSMOS field ($S_{1.1\mathrm{mm}} = 10.5 \pm 1.4$ mJy). Our high-resolution observations confirm that AzTEC2 splits into two components (namely AzTEC2-A and AzTEC2-B) for which we detect [C II] and ^{12}CO(5 → 4) line emission, implying a redshift of 4.626 ± 0.001 (4.633 ± 0.001) for AzTEC2-A (AzTEC2-B) and ruling out previous associations with a galaxy at $z \sim 1$. We use the ^{12}CO(5 → 4) line emission and adopt typical SMG-like gas excitation conditions to estimate the molecular gas mass, which is $M_{\mathrm{gas}}(\alpha_{\mathrm{CO}}/2.5) = 2.1 \pm 0.4 \times 10^{11}\,M_{\odot}$ for AzTEC2-A, and a factor four lower for AzTEC2-B. With the infrared-derived star formation rate of AzTEC2-A ($1920 \pm 100\,M_{\odot}\,\mathrm{yr}^{-1}$) and AzTEC2-B ($710 \pm 35\,M_{\odot}\,\mathrm{yr}^{-1}$), they both will consume their current gas reservoir within (30–200) Myr. We find evidence of a rotation-dominated [C II] disk in AzTEC2-A, with a deprojected rotational velocity of $v_{\mathrm{rot}}(i = 39°) = 660 \pm 130\ \mathrm{km\,s}^{-1}$, velocity dispersion $\lesssim$100 km s^{-1}, and dynamical mass of $M_{\mathrm{dyn}}(i = 39°) = 2.6^{+1.2}_{-0.9} \times 10^{11}\,M_{\odot}$. We propose that an elevated gas accretion rate from the cosmic web might be the main driver of the intense levels of star formation in AzTEC2-A, which might be further enhanced by gravitational torques induced by its minor companion (AzTEC2-B). These results strengthen the picture whereby the population of single-dish selected SMGs is rather heterogeneous, including a population of pairs of massive, highly active galaxies in a pre-coalescence phase.

Unified Astronomy Thesaurus concepts: Galaxies (573); Galaxy evolution (594); Galaxy formation (595); High-redshift galaxies (734); Disk galaxies (391)

1. Introduction

Empirical and theoretical evidence indicate that the global production of stars in galaxies is mainly regulated by the steady accretion of gas from the intergalactic medium (IGM; e.g., Dekel et al. 2009a; Hayward et al. 2012; LúHillier et al. 2012; Bouché et al. 2013), which drives widespread star formation in galactic disks over gigayear timescales (e.g., Daddi et al. 2010a; Genzel et al. 2010; Tacchella et al. 2016; Jiménez-Andrade et al. 2019). Such a process of galaxy evolution, known as the "cold gas accretion mode" of star formation, differs from the more intense production of stars during occasional starburst episodes of ten to a few hundred mega-years (Myr) length (e.g., Daddi et al. 2010a; Genzel et al. 2010; Rodighiero et al. 2011). This is often due to major/minor mergers providing the energetic and baryonic input to abruptly enhance the star formation rate (SFR) of galaxies (e.g., Narayanan et al. 2010; LúHillier et al. 2012; Ellison et al. 2013). Whereas both regimes of star formation have been widely explored out to intermediate redshifts ($z \sim 2$; e.g., Genzel et al. 2010; Wuyts et al. 2011; Magnelli et al. 2012, 2014; Daddi et al. 2015; Elbaz et al. 2018; Jiménez-Andrade et al. 2019), the relative role of the cold gas accretion and merger mode in driving the intense production of stars in galaxies at higher redshifts ($z \gtrsim 3$) remains an open issue (e.g., Carilli et al. 2010; Hayward et al. 2012, 2018; Hodge et al. 2012; Jiménez-Andrade et al. 2018; Tadaki et al. 2018).

Exploring such early cosmic epochs has been possible thanks to a strong, negative K-correction that makes high-redshift star-forming galaxies (SFGs) easier to detect at submillimeter wavelengths (e.g., Blain et al. 2002; Casey et al. 2014). These submillimeter-selected galaxies (SMGs) are, in general, massive star-bursting systems with SFR up to $\sim$2000 $M_{\odot}\,\mathrm{yr}^{-1}$ and stellar masses ($M_{\star}$) of $\log(M_{\star}/M_{\odot}) \gtrsim 10.5$ (e.g., Barger et al. 2012; Smolčić et al. 2015; Gómez-Guijarro et al. 2018; Harrington et al. 2018; Jiménez-Andrade et al. 2018; Lang et al. 2019). SMGs have acquired particular relevance for probing the merger and cold gas accretion mode in the yet unexplored $z \gtrsim 3$ regime (e.g., Carilli et al. 2010; Hayward et al. 2012). Although the "canonical" formation scenario of these massive starbursts involves major gas-rich mergers (e.g., Tacconi et al. 2006, 2008; Bothwell et al. 2010, 2013; Engel et al. 2010; Narayanan et al. 2010; Ivison et al. 2012), recent observational

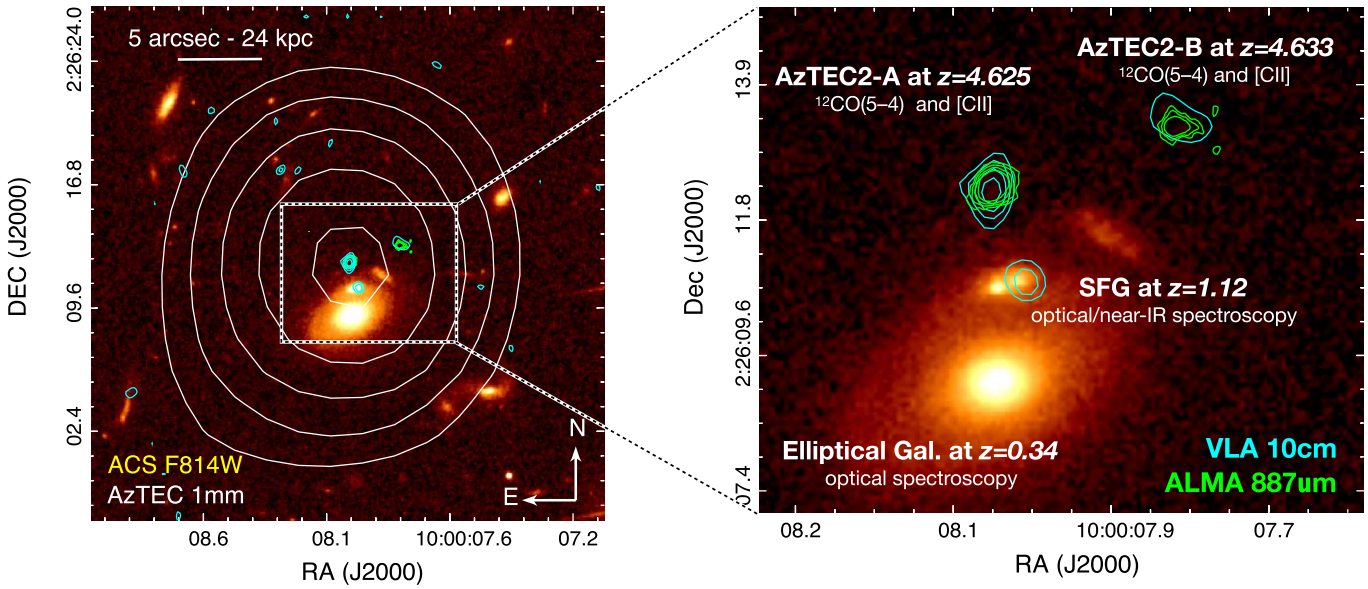

Figure 1. Multi-wavelength view toward the AzTEC2 source. Left panel: AzTEC/JCMT 1.1 mm (white Scott et al. 2008), ALMA Band 7/887μm (green; this study), and VLA Band S/10 cm (blue; Smolčić et al. 2017) contours overlaid on top of the *HST*/ACS F814W image. All contour levels are above three times the noise rms. The zoomed-in image (right panel) shows two foreground sources: a massive elliptical galaxy at $z = 0.34$ and a SFG at $z = 1.12$. ALMA and VLA imaging at subarcsecond resolution reveal two optically undetected components at $z \sim 4.63$, labeled AzTEC2-A and AzTEC2-B.

(and theoretical) evidence indicates that highly active star-forming disks can also lead to SMG-like luminosities (e.g., Davé et al. 2010; Hodge et al. 2012, 2016, 2019; Narayanan et al. 2015; Hayward et al. 2018; Tadaki et al. 2018).

A heterogeneous SMG population, i.e., secular disks and major mergers, could also explain the diversity of quiescent massive galaxies at $z \sim 2$–3 (e.g., Gobat et al. 2012; Toft et al. 2012, 2017). Whereas the structure and dynamics of most of those quiescent systems seem to be a result of compact, merger-driven SMGs at $z > 3$ (Toft et al. 2014; Ikarashi et al. 2015; Fudamoto et al. 2017; Gómez-Guijarro et al. 2018), the progenitors of quiescent disk galaxies at $z \sim 2$ (Newman et al. 2012; Toft et al. 2017) might have hosted enhanced star formation distributed across a massive rotating disk.

Despite the necessity of characterizing the properties of $z > 3$ massive, star-forming disks, only limited/small samples of such galaxies exist (e.g., Hodge et al. 2012; De Breuck et al. 2014; Jones et al. 2017; Shao et al. 2017). For instance, out of the 118 SFGs at $4 < z < 6$ in the recent ALPINE [C II] survey, no more than 15% of them are rotating disks (Le Fèvre et al. 2019). Among the hundreds of SMGs across the two square degree COSMOS field (e.g., Casey et al. 2013; Brisbin et al. 2017), only AzTEC1 ($z = 4.341$), AzTEC/C159 ($z = 4.569$), J1000+0234 ($z = 4.542$), and Vd−17871 ($z = 4.622$) exhibit convincing evidence for gas-dominated rotating disks (Jones et al. 2017; Tadaki et al. 2018). Consequently, these systems emerge as key laboratories to investigate the role of cold gas accretion in driving star formation at $z \sim 4.5$, which is the cosmic epoch when the cosmological gas accretion rate onto galaxies is expected to be maximal (e.g., Kereš et al. 2005).

Here, we use high-resolution observations of the Atacama Large Millimeter Array (ALMA) and NOrthern Extended Millimeter Array (NOEMA) to unveil the redshift and conditions for star formation in AzTEC2. This source is one of the brightest SMGs in the COSMOS field, which is composed of a massive, star-forming disk and a smaller companion galaxy at $z = 4.63$. We use [C II] and ^{12}CO(5 → 4) line observations to probe the gas content, star formation efficiency, and gas dynamics of AzTEC2 within the context of cold gas accretion and merger-driven star formation in the early universe. This manuscript is organized as follows. In Section 2, we introduce the AzTEC2 source, while in Section 3 we describe the observations and data reduction. In Section 4, we present the analysis and results. The implications of this work are discussed in Section 5. We adopt a flat ΛCDM cosmology with $h_0 = 0.7$, $\Omega_M = 0.3$, and $\Omega_\Lambda = 0.7$.

2. AzTEC2: A Bright, Multi-component SMG

AzTEC2 was originally identified in the two surveys undertaken with the camera AzTEC at 1.1 mm over an area of $\sim$0.5 degs^2 in the COSMOS field (Scott et al. 2008; Aretxaga et al. 2011). In the first survey, obtained with the camera AzTEC mounted at the James Clerk Maxwell Telescope, it was identified as the second brightest source in the survey: AzTEC2 (Scott et al. 2008). Later, with the camera AzTEC on the Atacama Submillimeter Telescope Experiment, it was identified as AzTEC/C3, i.e., the third brightest source in the survey (Aretxaga et al. 2011). This bright SMG was also detected in the deep Herschel/HerMES survey (250–500 μm maps) and SCUBA-2 at both 450 and 850 μm (Casey et al. 2013). AzTEC2 was recently cataloged as the second brightest SMG in the IRAM/GISMO 2 mm deep survey (over $\sim$250 arcmin^2, Magnelli et al. 2019) and as the brightest galaxy in the ALMA 2 mm mosaic in the COSMOS field (with an area of $\sim$155 arcmin^2; C. Casey et al. 2020, in preparation; J. Zavala et al. 2020, in preparation).

Recent imaging with ALMA (Brisbin et al. 2017) revealed that AzTEC2 is composed of two components separated by 3 arcsec (see Figure 1): namely component AzTEC2-A and AzTEC2-B. Both sources were also detected with a signal-to-noise ratio (S/N) > 10 in the 3 GHz radio continuum imaging with the Very Large Array (VLA) at 0.″75 resolution (Miettinen et al. 2017). Neither of the two components has a robust optical/near-infrared (IR) counterpart (Figure 1; Laigle

et al. 2016), hindering the redshift determination of the AzTEC2 complex. While a spectroscopic redshift solution of $z = 1.12$ has been adopted for AzTEC2 in past studies (e.g., Smolčić et al. 2012, 2017; Miettinen et al. 2015, 2017; Brisbin et al. 2017), recent optical/near-IR spectroscopy revealed that such a redshift value corresponds to a bright foreground SFG at only 1.″5 to the south of AzTEC2 (Casey et al. 2017; see our Figure 1). High-resolution observations at sub/millimeter wavelengths (probing the cold star-forming interstellar medium (ISM)) are hence crucial to unambiguously constrain the redshift of AzTEC2-A and AzTEC2-B, as well as to investigate the conditions for star formation in these bright SMGs.

3. Observations and Data Reduction

ALMA Band 7 observations (project 2015.1.00568.S, PI: C. Casey) were conducted on 2016 April 23 and September 1. The 12 m main array was used in two different configurations to obtain subarcsecond angular resolution without losing sensitivity at larger scales (maximum recoverable angular scale of ∼4.″7. The spectral setup, originally designed to only detect dust-continuum emission, covered the frequency ranges of 335.5–339.5 GHz and 347.5–351.5 GHz. Data reduction and imaging were performed following the standard steps of the ALMA reduction pipeline scripts with CASA. During the imaging process, a Briggs weighting (robust = 0.5) was used, since it provided a good compromise between angular resolution and noise. With ~ 590 s of integration time, we reached a final sensitivity of $1\sigma \simeq 1$ mJy beam^{-1} for a 50 MHz channel width (corresponding to ∼50 km s^{-1}) and a median restoring beam of 0.23×0.18 arcsec^2 (PA = 51°). These observations allow us to pinpoint the emission from the different sources in this crowded field, and to spatially resolve the emission of AzTEC2-A.

A preliminary analysis of the ALMA data revealed a serendipitous line detection at the edge of our spectral windows, which was associated with [C II] at $z \sim 4.6$ (see details in Section 4). To confirm the redshift, we then analyzed observations taken with the Redshift Search Receiver (Erickson et al. 2007) on the Large Millimeter Telescope. AzTEC2 was targeted as part of the Early Science Phase observations between 2014 and 2015 with a 32 m antenna (projects YUNM020 and HUGD024, PIs: M. Yun and D. Hughes, respectively). A total on-source time of 5 hr led to a noise rms of ≈1.0 mJy beam^{-1} per channel, with a spectral resolution of ∼31 MHz/100 km s^{-1} and spatial resolution of ∼25″. Data reduction was performed in a similar way as described in Zavala et al. (2015, 2018). The final spectrum, covering the frequency range 73−111 GHz, revealed a tentative detection of the ^{12}CO (5 → 4) line emission at $z \sim 4.6$. Although its low S/N (∼2) prevented us from firmly confirming the redshift, this tentative line detection allowed us to request further observations.

Follow-up observations were hence taken with NOEMA in Band 1 over two tracks on 2019 January 26 and 29 (project W18EU, PI: E.F. Jiménez-Andrade). A total observing time of 3.3 hr was reached using 10 antennas in A-configuration. We used the PolyFix correlator to cover the frequency range 84.9–92.7 GHz and 100.2–108.0 GHz, targeting the ^{12}CO(5 → 4) line at $z \sim 4.6$. The data reduction was performed with the software `GILDAS` using the NOEMA standard pipeline, while imaging was done with the package `mapping` using natural weighting. The achieved spatial resolution of 1.″7 × 0.″9 (PA = −163°) suffices to resolve the two components of AzTEC2 separated by ∼3″ (Figure 1). The spectral data cube was smoothed to a ∼34 MHz resolution (i.e., ∼100 km s^{-1}), reaching a sensitivity of 0.13 mJy beam^{-1} per channel.

4. Data Analysis and Results

4.1. Gravitational Lensing Magnification

Although there are no clear indications of gravitational amplification in our high-resolution ALMA data (Figure 2), there are two foreground galaxies that could magnify the emission of both AzTEC2 components (Figure 1). We use the `Visilens` code (Spilker et al. 2016) to estimate the gravitational amplification factor (μ) as follows. We model each foreground source separately, adopting a lens mass profile parameterized as an isothermal ellipsoid and assuming the Einstein mass to be $2.5M_\star$ (Auger et al. 2009). Given the relatively large offset between the foreground and background galaxies (≳1.″5), second-order parameters of the lens mass profiles such as shape and ellipticity are found to be not relevant for the analysis. At the position of both AzTEC2-A and AzTEC2-B, the foreground galaxy at $z = 1.1$ produces a negligible amplification while using a stellar mass upper limit of $\log(M_\star/M_\odot) = 9.6$. On the other hand, the amplification produced by the more massive, elliptical galaxy ($\log(M_\star/M_\odot) = 11$; Laigle et al. 2016) at $z = 0.34$ is estimated to be $\mu_A = 1.5$ ($\mu_B = 1.35$) at the position of AzTEC2-A (AzTEC2-B). We adopt these magnification factors throughout the rest of the paper.

4.2. ^{12}CO(5 → 4) and [C II] Line Detections in AzTEC2 at z = 4.6

The NOEMA spectrum reveals emission at the position of AzTEC2-A and AzTEC2-B peaking at ∼102.5 GHz. By collapsing the data cube within the frequency range 102.2–102.7 GHz, which encompasses the full emission line, we derive the intensity map shown in the upper right panel of Figure 2. A 2D Gaussian fit indicates that AzTEC2-A is resolved by our observations, with a deconvolved full width at half maximum of $\sqrt{\mu_A}$ FWHM = 1.″2 ± 0.″4 along the major axis. We use an aperture that is a factor 1.5 larger than the convolved FWHM of AzTEC2-A to retrieve most of the emission and extract the ^{12}CO(5 → 4) line spectrum. Since AzTEC2-B appears as a point-like (unresolved) source, we integrate emission across a region that equals the size of the synthesized beam to obtain the spectrum (lower-right panel of Figure 2). We identify a broad (FWHM ∼800 km s^{-1}), double-peaked emission line centered at 102.43 ± 0.03 GHz associated with AzTEC2-A. Through a least-squares algorithm (Levenberg–Marquardt), we find that a model with two Gaussian components better describes the line profile than a single Gaussian curve (yielding a reduced χ^2 of 2.0 and 2.6, respectively). We thus adopt the former model and derive an integrated flux density of $\mu_A S_{CO(5 \to 4)} = 1070 \pm 60$ mJy km s^{-1}. We also identify an 8.4σ line detection at the locus of AzTEC2-B that is centered at 102.30 ± 0.02 GHz. A single Gaussian model (reduced $\chi^2 = 1.2$) leads to an integrated flux density of $\mu_B S_{CO(5 \to 4)} = 260 \pm 30$ mJy km s^{-1} (Table 1).

By averaging line-free channel maps in the ^{12}CO(5 → 4) data cube, we also detect dust-continuum emission from both

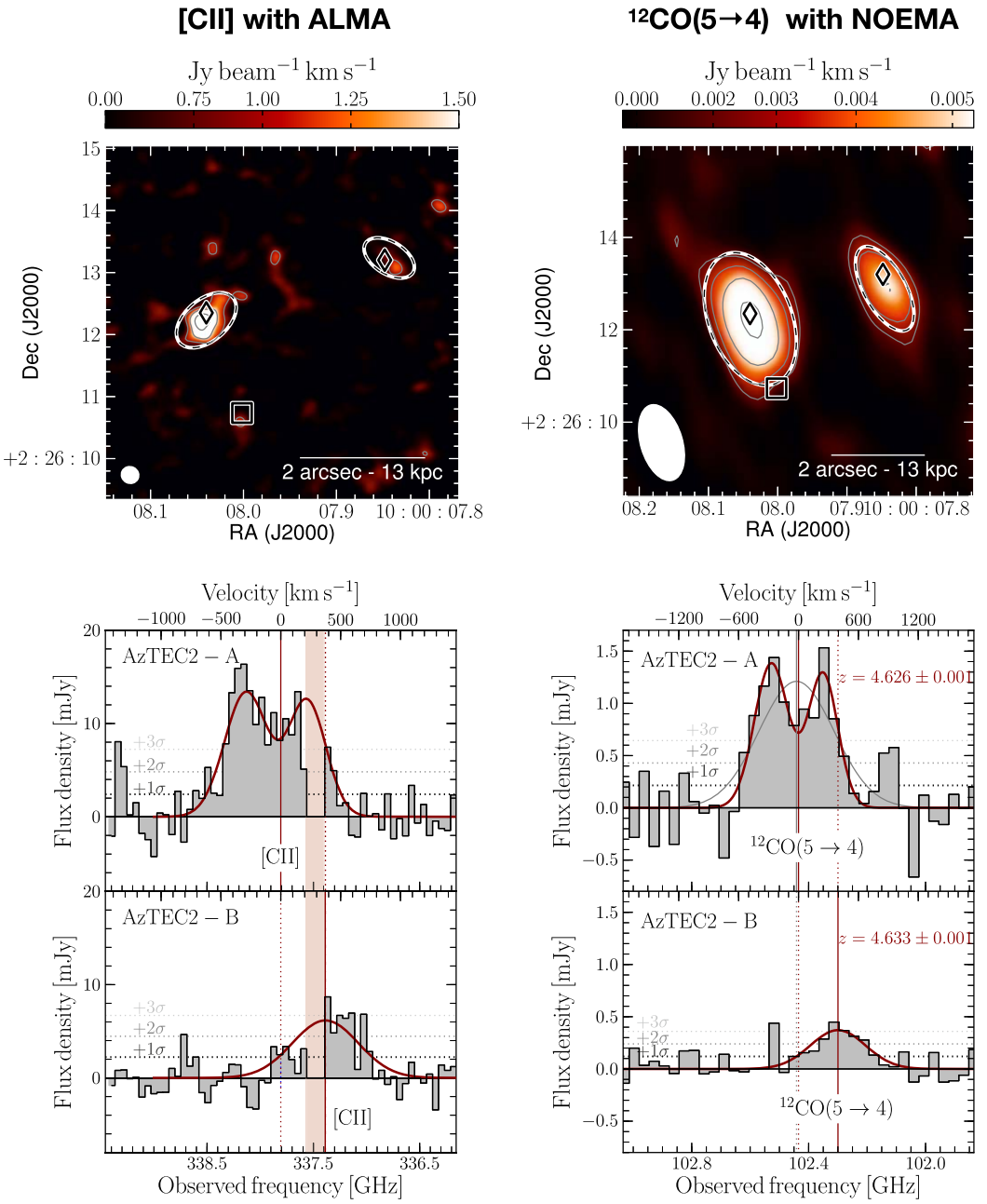

Figure 2. Upper panels: velocity-integrated intensity map ([−600, +1100] km s^{-1}) of the [C II] and ^{12}CO(5 → 4) line emission detected with ALMA and NOEMA, respectively, of AzTEC2-A and AzTEC2-B. The contours indicate the [3σ, 5σ, 8σ, 13σ] levels. The black diamonds mark the position of AzTEC2-A and AzTEC2-B inferred from high-resolution far-infrared and radio continuum imaging with ALMA and the VLA (Brisbin et al. 2017; Smolčić et al. 2017). The center of the foreground SFG at $z = 1.1235$ is marked by the black square. The synthesized beam is shown in the lower left corner, while the dashed ellipses illustrate the aperture used to extract the spectra. Lower panels: spectra of the [C II] and ^{12}CO(5 → 4) line emission detected with ALMA and NOEMA, respectively, of AzTEC2-A and AzTEC2-B. The red solid line represents the model with one (two) Gaussian component(s) that reproduce the [C II] and ^{12}CO(5 → 4) line profile in AzTEC2-B (AzTEC2-A). The gray line shows a Gaussian model to fit the ^{12}CO(5 → 4) line profile of AzTEC2-A. The vertical lines mark the central frequency of the [C II] and ^{12}CO(5 → 4) line profiles; in the case of AzTEC2-A, this is derived from a model with two (in red) and one (in gray) Gaussian component(s). The velocities displayed in the spectra are relative to the central frequency of the ^{12}CO(5 → 4) line emission in AzTEC2-A.

components (peak S/N $\gtrsim$ 10) at the observed wavelength of 2924 μm. A 2D Gaussian fitting gives a total flux density of 0.33 ± 0.05 mJy and 0.09 ± 0.02 mJy for AzTEC2-A and AzTEC2-B, correspondingly (Table 1). Limited by our 1.″7 × 0.″9 resolution, the dust-continuum emission of both components is not spatially resolved by these NOEMA observations.

Significant line emission is detected at ∼338 GHz toward both AzTEC2 components in the ALMA data cube (upper-left panel of Figure 2). The velocity-integrated intensity map shows that these sources are resolved. AzTEC2-A, in particular, exhibits extended emission distributed across ∼5 spatial resolution elements. A 2D Gaussian fit indicates a deconvolved FWHM of $\sqrt{\mu_A}$ FWHM = 0.″70 ± 0.″12 along the major axis for AzTEC2-A, and $\sqrt{\mu_B}$ FWHM = 0.″53 ± 0.″18 for AzTEC2-B (Table 1). To extract the line spectra we use an aperture that is a factor of 1.5 larger than the measured FWHM, allowing us to recover most of the extended line emission. As

Table 1
Properties of AzTEC2

Properties	Units	AzTEC2-A		AzTEC2-B	
		^{12}CO(5 → 4)	[C II]	^{12}CO(5 → 4)	[C II]
FWHM	km s^{-1}	890 ± 150	...	650 ± 150	...
Peak flux	mJy/beam	1.2 ± 0.2	13 ± 1	0.4 ± 0.1	6 ± 2
μ Integrated flux	Jy km s^{-1}	1.07 ± 0.06[a]	10.9 ± 1.2	0.26 ± 0.03[a]	4.2 ± 0.9
Central frequency	GHz	102.43 ± 0.03	337.8 ± 0.2	102.30 ± 0.02	337.4 ± 0.2
z[b]	...	4.626 ± 0.001		4.633 ± 0.001	
μ	...	1.5		1.35	
R.A., Decl.	hh:mm:ss.sss, dd:mm:ss.ss	10:00:08.042+02:26:12.19		10:00:07.842+02:26:13.32	
$\sqrt{\mu}\,\mathrm{FWHM}^{\mathrm{major-axis}}_{\mathrm{[C\,II]}}$	arcsec kpc^{-1}	0.70 ± 0.12/4.6 ± 1.0		0.53 ± 0.18/3.4 ± 1.2	
$\sqrt{\mu}\,\mathrm{FWHM}^{\mathrm{major-axis}}_{^{12}\mathrm{CO}(5\rightarrow4)}$	arcsec kpc^{-1}	1.2 ± 0.4/7.8 ± 2.6		...	
$\sqrt{\mu}\,\mathrm{FWHM}^{\mathrm{major-axis}}_{\mathrm{dust}}$	arcsec kpc^{-1}	0.36 ± 0.02/2.3 ± 0.1		0.35 ± 0.04/2.3 ± 0.3	
$\mu\,L_{\mathrm{IR}}$	$L_\odot$	(2.88 ± 0.13) × 10^{13}		(9.60 ± 0.45) × 10^{12}	
$\mu\,L_{\mathrm{FIR}}$	$L_\odot$	(1.20 ± 0.06) × 10^{13}		(0.40 ± 0.02) × 10^{13}	
$\mu\,L_{\mathrm{[C\,II]}}$	$L_\odot$	(3.09 ± 0.37) × 10^{10}		(1.17 ± 0.30) × 10^{10}	
$\mu\,L'_{\mathrm{CO}(5\rightarrow4)}$ [c]	K km s^{-1} pc^2	(4.1 ± 0.2) × 10^{10}		(1.0 ± 0.1) × 10^{10}	
$\mu\,L'_{\mathrm{CO}(1\rightarrow0)}$	K km s^{-1} pc^2	(12.8 ± 2.4) × 10^{10}		(3.1 ± 0.7) × 10^{10}	
$L_{\mathrm{IR}}/L'_{\mathrm{CO}(1\rightarrow0)}$	$L_\odot$(K km s^{-1} pc^2)$^{-1}$	220 ± 50		310 ± 80	
μ SFR	$M_\odot$ yr^{-1}	2880 ± 140		960 ± 45	
$\mu\,M_{\mathrm{gas}}(\alpha_{\mathrm{CO}}=0.8,\ \alpha_{\mathrm{CO}}=4.3)$	$M_\odot$	(1.0 ± 0.2, 5.5 ± 1.0) × 10^{11}		(0.25 ± 0.05, 1.3 ± 0.3) × 10^{11}	
$\mu\,M_{\mathrm{dust}}$	$M_\odot$	(3.2 ± 0.1) × 10^9		(1.07 ± 0.03) × 10^9	
$\tau_{\mathrm{gas}}(\alpha_{\mathrm{CO}}=0.8,\ \alpha_{\mathrm{CO}}=4.3)$	Myr	(35 ± 7, 190 ± 33)		(25 ± 6, 140 ± 30)	
$\mu\,S_{21\mathrm{cm}}$ [d]	mJy	0.045 ± 0.03		0.039 ± 0.02	
$\mu\,S_{10\mathrm{cm}}$ [e]	mJy	0.035 ± 0.06		0.025 ± 0.06	
$\mu\,S_{2924\mu\mathrm{m}}$	mJy	0.33 ± 0.05		0.09 ± 0.02	
$\mu\,S_{2000\mu\mathrm{m}}$ [f]	mJy		1.09 ± 0.22		
$\mu\,S_{1100\mu\mathrm{m}}$ [g]	mJy		11.5 ± 1.4		
$\mu\,S_{887\mu\mathrm{m}}$	mJy	13.3 ± 0.5		4.5 ± 0.5	
$\mu\,S_{850\mu\mathrm{m}}$ [h]	mJy		15.8 ± 1.6		
$\mu\,S_{500\mu\mathrm{m}}$ [i]	mJy		37.5 ± 3.7		
$\mu\,S_{350\mu\mathrm{m}}$ [i]	mJy		30.9 ± 3.5		
$\mu\,S_{250\mu\mathrm{m}}$ [i]	mJy		24.9 ± 2.5		
$\mu\,S_{160\mu\mathrm{m}}$ [j]	mJy		17.3 ± 7.1		
$\mu\,S_{100\mu\mathrm{m}}$ [k]	mJy		6.79 ± 2.50		
$\mu\,S_{24\mu\mathrm{m}}$ [k]	mJy		0.195 ± 0.019		

Notes.
[a] These observed flux densities will increase by a factor [1/0.8] when considering the effect of the CMB. We use the corrected value, i.e., $\mu\,S^{\mathrm{intrinsic}}_{\mathrm{CO}(5\rightarrow4)} = 1.34 \pm 10$ Jy km s^{-1} and 325 ± 40 mJy km s^{-1} for AzTEC2-A and AzTEC2-B, respectively.
[b] Redshift derived from ^{12}CO(5 → 4) line measurements.
[c] The effect of the CMB is considered when deriving this value (see Section 4.3).
[d] Schinnerer et al. (2010).
[e] Smolčić et al. (2017).
[f] Magnelli et al. (2019).
[g] Aretxaga et al. (2011).
[h] Geach et al. (2016).
[i] Oliver et al. (2012).
[j] Lutz et al. (2011).
[k] Le Floc'h et al. (2009).

illustrated in the lower left panel of Figure 2, these ALMA line detections lie at the edges of the spectral windows used in our observations, preventing us from recovering/inspecting their total line profiles. There is tentative evidence, however, of a double-peaked line profile in AzTEC2-A like that observed at ∼103 GHz with NOEMA. During the fitting procedure, the relative amplitude and FWHM of the two peaks from this ALMA [C II] line detection are fixed to the values of the ^{12}CO(5 → 4) line emission. The fit indicates a total integrated flux density of $\mu_{\mathrm{A}} S_{\mathrm{[C\,II]}} = 10.9 \pm 1.2$ Jy km s^{-1} and central frequency of 337.8 ± 0.2 GHz. On the other hand, we use the FWHM of our ∼103 GHz line detection as a prior to model the profile of that at ∼338 GHz in AzTEC2-B (reduced $\chi^2 = 0.9$), which gives a total integrated flux density of $\mu_{\mathrm{B}} S_{\mathrm{[C\,II]}} = 4.2 \pm 0.9$ Jy km s^{-1} and central frequency of 337.4 ± 0.2 GHz.

Finally, we average line-free channel maps in the [C II] data cube and detect dust-continuum emission for both AzTEC2 sources (peak $S/N \gtrsim 13$) at the observed wavelength of 887 μm (see Figure 1). By fitting a 2D Gaussian model we derive a total flux density of 13.3 ± 0.5 mJy and 4.5 ± 0.5 mJy for AzTEC2-A and AzTEC2-B, correspondingly (Table 1). The model also indicates that the dust-continuum emission of both components is spatially resolved by these ALMA observations, with a deconvolved FWHM of $\sqrt{\mu}$ FWHM $\simeq 0\farcs35 \pm 0\farcs03$ (Table 1).

By combining the line detections toward AzTEC2-A at ~102.5 and 337.5 GHz, we can unambiguously associate them with ^{12}CO(5 → 4) and [C II], respectively, leading to a redshift solution of $z = 4.626 \pm 0.001$. Similarly, for AzTEC2-B we estimate a redshift of $z = 4.633 \pm 0.001$, implying a velocity offset of $+375 \pm 50$ km s^{-1} with respect to AzTEC2-A. These robust line detections and counterpart associations rule out the preliminary redshift solution of $z = 1.1235$ for AzTEC2 adopted in past studies (e.g., Smolčić et al. 2012, 2017; Miettinen et al. 2015, 2017; Brisbin et al. 2017).

4.3. Molecular Gas Content and SFR of AzTEC2

We use the ^{12}CO(5 → 4) line detections to estimate the ^{12}CO(1→0) line luminosity, $L'_{\rm CO(1\,\rightarrow\,0)}$, and hence infer the molecular gas mass in the AzTEC2 complex. We first consider that due to the higher temperature of the cosmic microwave background (CMB) at $z = 4.6$, the intrinsic value of the ^{12}CO(5 → 4) line, $S^{\rm intrinsic}_{\rm CO(5\rightarrow4)}$, is a factor [1/0.8] higher (da Cunha et al. 2013) than the one measured from our observations. In using this factor, we assume that both AzTEC2-A and AzTEC2-B harbor a dense ISM with elevated gas kinetic temperature ($T_{\rm kin} \sim 40$ K)—as the majority of SMGs (e.g., Magnelli et al. 2012; Yang et al. 2017; Cañameras et al. 2018). Therefore, we find that $\mu\, S^{\rm intrinsic}_{\rm CO(5\rightarrow4)}$ is 1340 ± 100 mJy km s^{-1} (325 ± 40 mJy km s^{-1}) for AzTEC2-A (AzTEC2-B). The corresponding line luminosity is subsequently derived following Carilli & Walter (2013, Section 2.4). We adopt typical SMG-like gas excitation conditions to convert the ^{12}CO(5 → 4) line luminosity, $L'_{\rm CO(5\rightarrow4)}$, to $L'_{\rm CO(1\rightarrow0)}$. Then, $L'_{\rm CO(1\rightarrow0)} = [1/0.32] \times L'_{\rm CO(5\rightarrow4)}$ (e.g., Bothwell et al. 2013; Carilli & Walter 2013), which gives $\mu\, L'_{\rm CO(1\rightarrow0)} = 12.8 \pm 2.4 \times 10^{10}$ K km s^{-1} pc^2 and $3.1 \pm 0.7 \times 10^{10}$ K km s^{-1} pc^2 for AzTEC2-A and AzTEC2-B, respectively (see Table 1). Finally, the molecular gas mas, $M_{\rm gas}$, can be inferred through the CO-to-H$_2$ ($\alpha_{\rm CO}$) conversion factor: $M_{\rm gas} = \alpha_{\rm CO} L'_{\rm CO(1\rightarrow0)}$. The value of $\alpha_{\rm CO}$ depends on the physical and chemical conditions of the ISM (e.g., Papadopoulos et al. 2012a, 2012b). While low values ($\alpha_{\rm CO} = 0.8\, M_\odot$ K^{-1} km^{-1} s pc^{-2}) are consistent with the turbulent and extreme ISM conditions of, for example, ultraluminous infrared galaxies (ULIRGs; e.g., Downes & Solomon 1998), higher values ($\alpha_{\rm CO} = 4.3\, M_\odot$ K^{-1} km^{-1} s pc^{-2}) are consistent with a self-gravitating gas configuration as observed in star-forming disks (e.g., Magnelli et al. 2012). Here we adopt a mean $\alpha_{\rm CO} = 2.5\, M_\odot$ K^{-1} km^{-1} s pc^{-2}[11] to better compare AzTEC2-A and AzTEC2-B with the heterogeneous population of $z \sim 4$–5 SMGs, which includes both mergers and star-forming disks (e.g., Hayward et al. 2018). We find a molecular gas mass of $\mu_{\rm A}\, M_{\rm gas}(\alpha_{\rm CO}/2.5) = (3.2 \pm 0.6) \times 10^{11} M_\odot$ in AzTEC2-A, and a factor of four lower in AzTEC2-B (see Table 1). The lensing-corrected gas mass budget of AzTEC2-A, $M_{\rm gas}(\alpha_{\rm CO}/2.5) = (2.1 \pm 0.4) \times 10^{11} M_\odot$, is consistent with the massive gas reservoir of other $z \sim 4$–5 SMGs like AzTEC1, AzTEC3, AzTEC/C159, J1000+0234, and GN20 (Schinnerer et al. 2008; Carilli et al. 2010; Riechers et al. 2010; Hodge et al. 2012; Yun et al. 2015; Jiménez-Andrade et al. 2018; Tadaki et al. 2018), for which the median $M_{\rm gas}(\alpha_{\rm CO}/2.5)$ is $\sim 2 \times 10^{11} M_\odot$.

[11] We refer the reader to Section 5.2 where we discuss the nature of $\alpha_{\rm CO}$ in more detail.

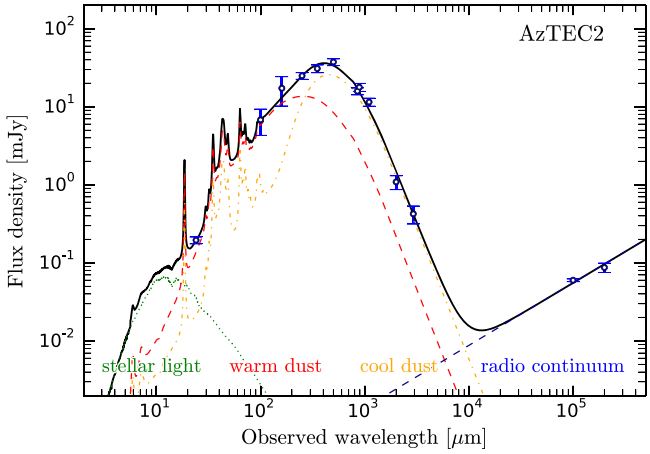

Figure 3. Broadband SED of AzTEC2. The monochromatic flux densities (blue circles) used in the fit correspond to the total emission from both components (see values in Table 1). The best-fit model is given by the black thick line. The dashed red (dash-doted orange) line shows the model of the warm (cool) dust emission. The stellar emission is shown by the dotted green line, while the radio continuum emission is represented by the dashed blue line.

We derive the infrared luminosity ($L_{\rm IR}$, integrated over the wavelength range of 8–1000 μm) and dust mass ($M_{\rm dust}$) of the AzTEC2 complex by fitting its mid-IR–to–millimeter SED (see Figure 3). This is done by following the spectral energy distribution (SED) fitting procedure presented by Liu et al. (2018), and by combining our dust-continuum measurements at 887 and 2.92 mm with information from the COSMOS photometric catalog compiled by Jin et al. (2018) and Liu et al. (2018). In the case of AzTEC2, this catalog includes photometric measurements at (see Table 1): 24 μm (Le Floc'h et al. 2009), 100 μm, 160 μm (Lutz et al. 2011), 250 μm, 350 μm, 500 μm (Oliver et al. 2012), 850 μm (Geach et al. 2016), 1.1 mm (Aretxaga et al. 2011), 10 cm (Schinnerer et al. 2010), and 21 cm (Smolčić et al. 2017). The photometric measurement at 2 mm recently obtained with the GISMO-2 bolometer camera (Magnelli et al. 2019) is also included in the analysis.

Since most photometric data toward the AzTEC2 complex do not have sufficient resolution to deblend the emission of AzTEC2-A and AzTEC2-B (Table 1), we use the combined monochromatic flux densities of both components even if high-resolution observations are available. We then fit the SED with five components: a stellar template from the Bruzual & Charlot (2003) models, an active galactic nuclei (AGN) template from Mullaney et al. (2011), and warm and cold dust templates from Draine & Li (2007). The fifth component is a radio power law tailored to the dust IR luminosity with $q_{\rm IR} = 2.4$, where $q_{\rm IR}$ is the median value for the ratio between far-infrared and radio luminosity of SFGs (e.g., Magnelli et al. 2015; Delhaize et al. 2017). The fitting is performed through Monte Carlo sampling

(with $N = 15{,}000$, following Liu et al. 2018), from which the χ^2 distribution and uncertainties are obtained. Our analysis indicates that a model with no AGN component provides the best fit to our data points, albeit more photometric information is needed to confirm the (apparently) negligible AGN activity in AzTEC2. Finally, we derive a total infrared luminosity of $\log(\mu L_{\rm IR}/L_\odot) = 13.59 \pm 0.02$ and dust mass of $\log(\mu M_{\rm dust}/M_\odot) = 9.64 \pm 0.10$ for the AzTEC2 complex.

To disentangle the contribution of AzTEC2-A and AzTEC2-B to the total $L_{\rm IR}$ and $M_{\rm dust}$, we use our high-resolution photometric data at 887 and 2924 μm. These observations independently trace the peak and Rayleigh–Jeans regime of the SED of both components (Table 1), allowing us to infer the contribution of AzTEC2-A and AzTEC2-B to the total IR SED. Then, since the ratio between the IR flux density of the two components at 887 and 2924 μm is $S^{\rm IR}_{\rm AzTEC2\text{-}A}/S^{\rm IR}_{\rm AzTEC2\text{-}B} \simeq 3$, we estimate $\log(\mu_{\rm A} L_{\rm IR}/L_\odot) = 13.46 \pm 0.02$ and $\log(\mu_{\rm A} M_{\rm dust}/M_\odot) = 9.51 \pm 0.10$ for AzTEC2-A. For AzTEC2-B we derive $\log(\mu_{\rm B} L_{\rm IR}/L_\odot) = 12.98 \pm 0.02$ and $\log(\mu_{\rm B} M_{\rm dust}/M_\odot) = 9.03 \pm 0.10$.

We note that the above reasoning assumes that the intrinsic SEDs of AzTEC2-A and AzTEC2-B are similar. While this is supported by the consistent flux density ratios at 887 and 2924 μm, the properties that have been inferred from the scaled SEDs are subject to a high degree of uncertainty. Therefore, to add an independent constraint on the $L_{\rm IR}$ of AzTEC2-A and AzTEC2-B that is not affected by source blending, we use their [C II] line luminosity ($L_{\rm [C\,II]}$) to estimate $L_{\rm IR}$ via the empirical $L_{\rm [C\,II]}/L_{\rm IR}$ luminosity ratio (e.g., Maiolino et al. 2009; Lagache et al. 2018). We assume that the physical properties of AzTEC2-A and AzTEC2-B are similar to the ones of bright SMGs at similar redshifts ($4 < z < 5$), for which $L_{\rm [C\,II]}/L_{\rm IR} = 7^{+4}_{-2} \times 10^{-4}$ (see the compilation in Table B.1 of Lagache et al. 2018). With $\log(\mu_{\rm A} L_{\rm [C\,II]}/L_\odot) = 10.49 \pm 0.05$, we estimate $\log(\mu_{\rm A} L_{\rm IR}/L_\odot) = 13.48 \pm 0.14$ for AzTEC2-A. Likewise, for AzTEC2-B we find $\log(\mu_{\rm B} L_{\rm [C\,II]}/L_\odot) = 10.07 \pm 0.10$ and $\log(\mu_{\rm B} L_{\rm IR}/L_\odot) = 13.07 \pm 0.17$. Although here we neglect possible differences in the $L_{\rm [C\,II]}/L_{\rm IR}$ ratio of AzTEC2-A and AzTEC2-B arising from distinct physical conditions of the ISM (e.g., ultraviolet radiation field and/or metal enrichment; Katz et al. 2017; Rybak et al. 2019), these new and independent $L_{\rm IR}$ estimates corroborate those derived via SED fitting.

We infer the SFR of both components following the calibration from Kennicutt (1998): SFR[$M_\odot$ yr^{-1}] $=10^{-10} L_{\rm IR}$ [$L_\odot$]. Assuming a Chabrier Initial Mass Function, we derive $\mu_{\rm A}$ SFR $= 2880 \pm 140\, M_\odot$ yr^{-1} for AzTEC2-A, while for AzTEC2-B we find $\mu_{\rm B}$ SFR $= 960 \pm 45\, M_\odot$ yr^{-1}. The lensing-corrected SFR of AzTEC2-B ($710 \pm 35\, M_\odot$ yr^{-1}) is consistent with the average for SMGs at similar redshifts ($\sim$800 $M_\odot$ yr^{-1}; e.g., Smolčić et al. 2015; Gómez-Guijarro et al. 2018; Jiménez-Andrade et al. 2018; Magnelli et al. 2019). The extreme IR-based SFR of AzTEC2-A (SFR $= 1920 \pm 100\, M_\odot$ yr^{-1}) is comparable to those of the massive, star-forming disks GN20 and AzTEC1 at $z \sim 4.5$ (Carilli et al. 2010; Magnelli et al. 2012; Tadaki et al. 2018).

On the other hand, we use our $M_{\rm dust}$ estimates to infer the molecular gas mass of AzTEC2-A and AzTEC2-B. We assume that these SMGs have solar metallicity, and consequently that they harbor a gas-to-dust ratio of $\delta_{\rm GDR} \sim 100$ (following the $\delta_{\rm GDR}$—metallicity relation derived by Leroy et al. 2011). Then,

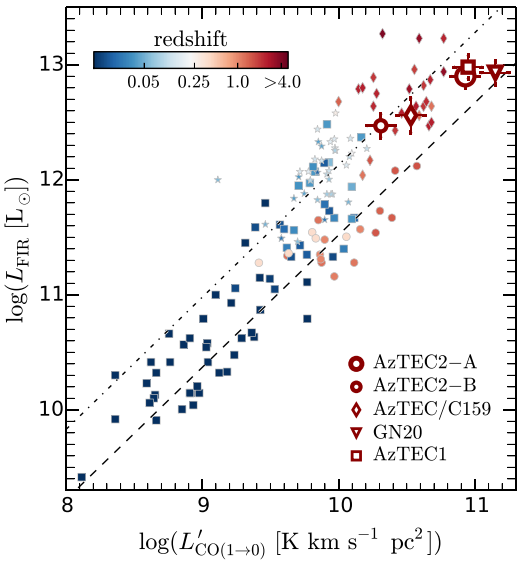

Figure 4. FIR luminosity as a function of ^{12}CO(1→0) line luminosity for local and high-redshift SFGs. The squares represent nearby normal and starburst galaxies reported by Gao & Solomon (2004), while stars correspond to low-redshift ULIRGs in the sample of Solomon et al. (1997). The circles show $z \sim 1.5$ star-forming disks presented in Daddi et al. (2010a), Geach et al. (2011) and Magnelli et al. (2012). The diamonds represent the parameter space covered by the SMGs reported in Bothwell et al. (2013). The large symbols correspond to the SMGs studied here and the massive, rotating disk galaxies at $z \sim 4.5$: GN20, AzTEC1, and AzTEC/C159 (Carilli et al. 2010; Hodge et al. 2012; Jones et al. 2017; Jiménez-Andrade et al. 2018; Tadaki et al. 2018). In the case of AzTEC2-A and AzTEC2-B, we use lensing-corrected luminosities. If only $L_{\rm IR}$ measurements are available in the literature, we convert $L_{\rm IR}$ into $L_{\rm FIR}$ by considering that $\langle \log(L_{\rm IR}) \rangle = 0.3 + \langle \log(L_{\rm FIR}) \rangle$ (e.g., Delhaize et al. 2017). The dashed and dotted lines show the best-fitting relation for MS and starburst galaxies, respectively, reported by Genzel et al. (2010).

$\log(\mu_{\rm A} M_{\rm gas}/M_\odot) \simeq \log(\mu \delta_{\rm GDR} M_{\rm dust}/M_\odot) = 11.5 \pm 0.1$ for AzTEC2-A and $\log(\mu_{\rm B} M_{\rm gas}/M_\odot) = 11.0 \pm 0.1$ for AzTEC2-B. These values are in good agreement with the $M_{\rm gas}$ estimates derived from our ^{12}CO (5 → 4) line observations assuming a mean $\alpha_{\rm CO}$ of $2.5\, M_\odot$ K^{-1} km^{-1} s pc^{-2}, which are $\log(\mu\, M_{\rm gas}/M_\odot) = 11.50 \pm 0.05$ and 10.90 ± 0.05 for AzTEC2-A and AzTEC2-B, correspondingly.

4.4. Mode of Star Formation in AzTEC2

The $L_{\rm IR}/L'_{\rm CO(1\to0)}$ ratio gives an indication of how efficient the production of stars in galaxies is for a given molecular gas reservoir. We estimate a $L_{\rm IR}/L'_{\rm CO(1\to0)}$ ratio of 220 ± 50 $L_\odot$(K km s^{-1} pc^2)$^{-1}$ for AzTEC2-A and $300 \pm 85\, L_\odot$(K km s^{-1} pc^2)$^{-1}$ for AzTEC2-B (see Table 1). The star formation efficiency of AzTEC2-A is larger than those of nearby and $z \sim 2$ star-forming disks (20–100 $L_\odot$(K km s^{-1} pc^2)$^{-1}$; Daddi et al. 2010a; Genzel et al. 2010), but it is in agreement with the $L_{\rm IR}/L'_{\rm CO(1\to0)}$ ratio of $z \sim 4.5$ star-forming disks like GN20 and AzTEC/C159 (180−220 $L_\odot$(K km s^{-1} pc^2)$^{-1}$; Hodge et al. 2012; Jiménez-Andrade et al. 2018).

To better compare the star formation efficiency of AzTEC2-A and AzTEC2-B with respect to the overall SFG's population, in Figure 4 we present the $L_{\rm FIR} - L'_{\rm CO(1\to0)}$ relation for star-forming disks and merger-driven starbursts derived by Genzel et al. (2010). For this exercise, we estimate the far-IR (FIR) luminosity ($L_{\rm FIR}$) of the AzTEC2 complex by integrating the total IR SED (Figure 3) over the wavelength range 42.5–122.5 μm (following Helou et al. 1985). Then, the $L_{\rm FIR}$

of AzTEC2-A and AzTEC2-B are inferred from the relative ratio of their dust-continuum flux density at 887 and 2924 μm (as done for $L_{\rm IR}$ in Section 4.3). We estimate $\log(\mu_{\rm A} L_{\rm FIR}/L_{\odot}) = 13.08 \pm 0.02$ for AzTEC2-A, and $\log(\mu_{\rm B} L_{\rm FIR}/L_{\odot}) = 12.60 \pm 0.02$ for AzTEC2-B (see Table 1). Combining these values with our $L'_{\rm CO(1\rightarrow0)}$ estimates, we plot the locus of AzTEC2-A and AzTEC2-B in the $L_{\rm FIR} - L'_{\rm CO(1\rightarrow0)}$ plane. We also include compilations of nearby normal and starburst galaxies (Solomon et al. 1997; Gao & Solomon 2004), $z \sim 1.5$ star-forming disks (Daddi et al. 2010a; Geach et al. 2011; Magnelli et al. 2012), SMGs (Bothwell et al. 2013), and massive star-forming disks at $z \sim 4.5$ (Carilli et al. 2010; Hodge et al. 2012; Jones et al. 2017; Jiménez-Andrade et al. 2018; Tadaki et al. 2018). This comparison indicates that most of the reported SMGs, like AzTEC2-B, lie on/above the empirical $L_{\rm FIR} - L'_{\rm CO(1\rightarrow0)}$ relation for mergers. Despite being at the high end of the $L_{\rm FIR} - L'_{\rm CO(1\rightarrow0)}$ plane, AzTEC2-A (as well as GN20 and AzTEC1) approaches the relation of normal, star-forming disk galaxies (see Figure 4; e.g., Genzel et al. 2010).

Another indicator of star formation efficiency is the $L_{\rm IR}/L'_{\rm CO(5\rightarrow4)}$ ratio (e.g., Daddi et al. 2015), which traces the dense, warm molecular gas ($n > 10^4$ cm^{-3}) that is closely linked to massive star formation. We find that AzTEC2-A (AzTEC2-B) exhibits a ratio that is 1.6 (2.5) larger than local star-forming and $z \sim 1.5$ main sequence (MS) galaxies (e.g., Liu et al. 2015). This suggests that AzTEC2-A consumes its star-forming gas faster than secular star-forming disks, but at a more moderate rate than typical SMGs like AzTEC2-B.

Given their available gas reservoir, AzTEC2-A (AzTEC2-B) will be able to sustain their current SFR for a period of $\sim$110 Myr (80 Myr) (assuming a mean $\alpha_{\rm CO} = 2.5\,M_{\odot}$ K^{-1} km^{-1} s pc^{-2}). The gas depletion timescale ($\tau_{\rm gas}$) of AzTEC2-A, in particular, exhibits a mild excess with respect to the average for SMGs at similar redshifts ($\tau_{\rm gas} \sim 45$ Myr; Aravena et al. 2016), but resembles one of the massive, star-forming disk galaxies GN20, AzTEC/C159 and AzTEC1 at $z \sim 4.5$ (Hodge et al. 2012; Jiménez-Andrade et al. 2018; Tadaki et al. 2018).

Overall, the properties of AzTEC2-A and AzTEC2-B are consistent with the intense star formation activity observed in bright SMGs at $z \sim 4$ (Schinnerer et al. 2008; Riechers et al. 2010; Yun et al. 2015; Jiménez-Andrade et al. 2018; Tadaki et al. 2018). AzTEC2-A resembles—to some extent—the properties of massive, star-forming disks at lower and similar redshifts (e.g., Daddi et al. 2010a; Genzel et al. 2010; Hodge et al. 2012), which form stars through the cold gas accretion mode of star formation.

4.5. A Rapidly Rotating, Massive Disk in AzTEC2-A

Predictions from numerical simulations (e.g., Kohandel et al. 2019) and observations of high-redshift galaxies (e.g., Jones et al. 2017) have suggested that a double-peaked [C II] line profile, like that of AzTEC2-A (Figure 2), can be consistent with a rotating disk galaxy. We then use the high-resolution [C II] line observations to explore the kinematics of AzTEC2-A, for which the high S/N of the detection enables us to derive the velocity field and velocity dispersion of the gas. As observed in Figure 5, AzTEC2-A exhibits a smooth velocity gradient that appears to be consistent with rotationally dominated kinematics. To parameterize its motion, we derive the position–velocity (pv) diagram (Figure 5) along the major axis of the [C II] line emission using a 0.″3 width aperture.

There exist several parameterizations (or models) that can describe the rotation curves of galaxies, including the basic two-parameter arctan function, the more elaborate "multi-parameter function" (Courteau 1997), and the physically motivated "universal rotation curve" model (Persic et al. 1996). The empirically motivated arctan model is given by $v(r) = (2/\pi)\,v_{\rm asym}\arctan(r/r_{\rm t})$ (e.g., Courteau 1997; Willick 1999), where $v_{\rm asym}$ is the asymptotic rotational velocity and $r_{\rm t}$ is the transition radius between the rising and flat part of the rotation curve. With only two free parameters, the arctan function provides an adequate description to rotation curves of low- and high-redshift galaxies (Courteau 1997; Willick 1999; Miller et al. 2011; Swinbank et al. 2012; De Breuck et al. 2014; Drew et al. 2018).

We thus adopt the arctan model to fit the rotation curve of AzTEC2-A. As observed in Figure 5, this function offers a reasonable description of the observed portion of the PV diagram. Our fit, limited by the lack of velocity channels above $+200$ km s^{-1}, suggests an asymptotic velocity of 415 ± 70 km s^{-1} and $\mu_{\rm A}\, r_{\rm t} = 0.7 \pm 0.1$ kpc. To derive the intrinsic (deprojected) rotational velocity, $v_{\rm rot}^{\rm int} = v_{\rm rot}/\sin(i)$, we need to infer the disk inclination (i). This can be derived from the apparent ellipticity of the galaxy: i.e., $i = \arcsin({\rm FWHM_{minor}}/{\rm FWHM_{major}})$, where the respective FWHM values can be derived from the surface brightness distribution of the [C II] line. However, as observed in Figure 5, the absence of velocity channels above $+200$ km s^{-1} biases the spatial distribution of the [C II] line emission. Assuming a cospatial distribution of interstellar dust and gas, the inclination of the [C II] disk can be approximated from the ellipticity of the dust-continuum emission revealed by our high-resolution ALMA observations (Section 4.2). We then derive $i = \arcsin(0.23 \pm 0.02/0.36 \pm 0.02) = 39° \pm 3°$, which leads to an intrinsic rotational velocity of $v_{\rm rot}^{\rm int} = v_{\rm asym} = 660 \pm 130$ km s^{-1}. Such a high rotational speed is consistent with one of the rapidly spinning, star-forming disks GN20, AzTEC/C159, and J1000+0234 at $z \sim 4.5$ ($\gtrsim$500 km s^{-1}; Carilli et al. 2010; Hodge et al. 2012; Jones et al. 2017).

To evaluate the rotational-to-dispersion support ($v_{\rm rot}/\sigma$) of the disk, we inspect the line-of-sight velocity dispersion (σ) map in Figure 5. We anticipate that at the innermost region of the galaxy, the measured σ is highly enhanced by "beam smearing"[12] (e.g., Davies et al. 2011; Stott et al. 2016). Since such a contribution is expected to be modest at the outermost radii, we adopt 100 km s^{-1} (from the contour levels in the map, Figure 5) as an upper limit for the intrinsic velocity dispersion of the gas in the disk. Then, we derive $v_{\rm rot}/\sigma \gtrsim 5$, indicating that AzTEC2-A is rather an unperturbed, rotation-dominated disk that resembles the $v_{\rm rot}/\sigma$ ratio of more evolved disk galaxies at $z \sim 1$ (e.g., Di Teodoro et al. 2016, and references therein). This finding, therefore, provides more evidence of kinematically mature disks that can be found at even $z \sim 4.5$, such as GN20 (Hodge et al. 2012), ALESS 73.1 (De Breuck et al. 2014), AzTEC/C159, J1000+0234, (Jones et al. 2017; Jiménez-Andrade et al. 2018), and AzTEC1 (Tadaki et al. 2018).

[12] At the innermost region of galaxies, the measured line width is boosted by large-scale motions occurring within the region traced by a relatively coarse (finite) point-spread function (PSF).

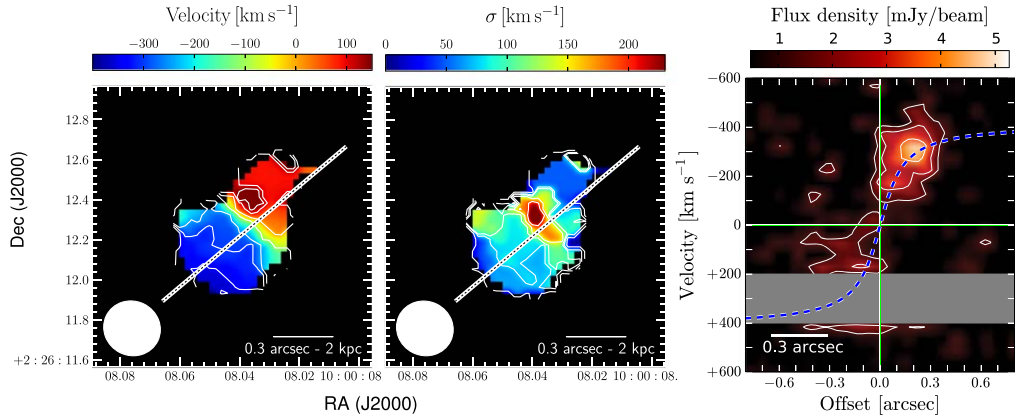

Figure 5. Velocity field (left panel) and velocity dispersion (central panel) of the gas in AzTEC2-A ($z = 4.626$), derived from [C II] line observations with ALMA. Note that the velocity channels above 200 km s^{-1} are not available in the data set (see Figure 2). The contour levels are at [−350, −300, −250, −100, 0, 100, 150] km s^{-1} and [25, 75, 100, 150, 200] km s^{-1} for the velocity field and velocity dispersion maps, respectively. The synthesized beam is shown in the lower left corner. The pv diagram (right panel) has been extracted using a 0.″3 width aperture along the galaxy's major axis (position angle of −40°; black dashed line). The blue dashed line is a simple arctan model to describe the rotation curve of AzTEC2-A. The contour levels are at 3, 5, and 8 times the rms noise. The gray shaded region shows the velocity range that is not available in the current data set. The horizontal bar shows the major axis of the synthesized beam.

Finally, by assuming that the kinematics of the disk is mainly dominated by the gravitational potential of AzTEC2-A, its dynamical mass ($M_{\rm dyn}$) can be estimated through the relation: $M_{\rm dyn}\sin^2(i) = Rv(R)^2/G$, where $v(R)$ is the rotation velocity at radius R and G is the gravitational constant. Using $R = 0.''5$ that encompasses the full extent of the [C II] line emission, and that equals the size of the aperture used to obtain the spectrum, we find $M_{\rm dyn}(i = 39°) = 2.6^{+1.2}_{-0.9} \times 10^{11} M_\odot$. This mass budget roughly agrees with that expected for the molecular gas mass ([0.7, 3.7] $\times$ 10^{11} $M_\odot$), indicating that AzTEC2-A is a massive gas-rich disk possibly assembled through an enhanced accretion of gas from the cosmic web (e.g., Bournaud & Elmegreen 2009; Dekel et al. 2009a, 2009b; Romano-Díaz et al. 2014). A post-merger scenario, however, cannot be excluded, given that disks could survive or re-form rather quickly after a gas-rich merger (e.g., Springel & Hernquist 2005; Hammer et al. 2009; Hopkins et al. 2009). Simulated disk galaxies that formed via gas-rich mergers can resemble the observed properties (kinematics, SFR, gas surface density) of $z \sim 2$ disks (Robertson & Bullock 2008). Furthermore, a coarse PSF (like ours, $\gtrsim$1 kpc) diminishes the contrast between disturbed kinematics and rotation-dominated disks (Hung et al. 2016). Deeper [C II] line observations with subkiloparsec scale resolution are thus needed to accurately derive the kinematic properties of AzTEC2-A and hence to isolate the formation scenario of its rotating gas disk.

5. Implications for Galaxy Evolution at High Redshift

The redshift identification and subsequent dynamical characterization of AzTEC2-A add new supporting evidence for the existence of massive vigorously star-forming disks in the early universe. By including AzTEC2-A, the sample of SMGs at $4 < z < 5$ with robust evidence of rotation has now increased to seven sources: AzTEC2-A, AzTEC/C159, AzTEC1, Vd-17871, J1000+0234, ALESS 73.1, and GN20 (Carilli et al. 2010; Hodge et al. 2012; De Breuck et al. 2014; Jones et al. 2017; Tadaki et al. 2018). The former galaxies represent more than half the population of spectroscopically confirmed $z > 4$ SMGs within the two square degrees of the COSMOS field (Smolčić et al. 2012, 2015). Here, we discuss the implications of these findings within the context of cold gas accretion and merger-driven star formation in massive, high-redshift galaxies.

5.1. A Heterogeneous SMG Population

The enhanced production of stars in SMGs has been largely attributed to gas-rich galaxy mergers (e.g., Tacconi et al. 2008; Engel et al. 2010; Younger et al. 2010; Riechers et al. 2011; Iono et al. 2016), which is compatible with the merger-driven starbursts in local ULIRGs (e.g., Sanders & Mirabel 1996). In the case of AzTEC2, and as observed in Figure 1, our current ALMA dust-continuum imaging does not reveal clear signs of disturbance/interaction between AzTEC2-A and AzTEC2-B (e.g., strong tidal tails and/or bridges). Although this could be a result of the surface brightness limit of these observations, the clear spatial separation between AzTEC2-A and AzTEC2-B ($\sim$20 kpc) and the relative velocity offset of 350 km s^{-1} suggest that these galaxies undergo a pre-coalescence (first approach) phase (e.g., Calderón-Castillo et al. 2019). This might indicate that the vigorous SFR in AzTEC2-A is not dominated by merging activity. Instead, the gas velocity fields, $L_{\rm FIR}/L'_{\rm CO(1\rightarrow0)}$, and $L_{\rm IR}/L'_{\rm CO(5\rightarrow4)}$ ratio point toward a smoother mode of star formation that drives a massive, star-forming disk (e.g., Dekel et al. 2009a, 2009b; Carilli et al. 2010; Hodge et al. 2012; Romano-Díaz et al. 2014). Certainly, the properties of AzTEC2 resemble those of the well-characterized star-forming disk GN20 at similar redshift (Carilli et al. 2010; Hodge et al. 2012).

These results strengthen the scenario in which single-dish-selected SMGs are a heterogeneous population (e.g., Hayward et al. 2011, 2013), including major mergers (e.g., Engel et al. 2010; Riechers et al. 2014), isolated disk galaxies, and pairs of (likely infalling) galaxies that are blended into a single submillimeter source as observed in AzTEC2. As discussed by Hayward et al. (2011), this heterogeneity is linked to the SMG selection function. Since submillimeter surveys lead to flux ($\propto$SFR) limited samples of galaxies (e.g., Scott et al. 2008; Aretxaga et al. 2011), at high redshift ($z \gtrsim 3$), only SFGs harboring a SFR $\gtrsim$ 300 $M_\odot$ yr^{-1} can be selected with typical single-dish surveys (e.g., Magnelli et al. 2019). Therefore, this selection function tends to identify the extreme and massive end of the SFG population at high redshifts, including both

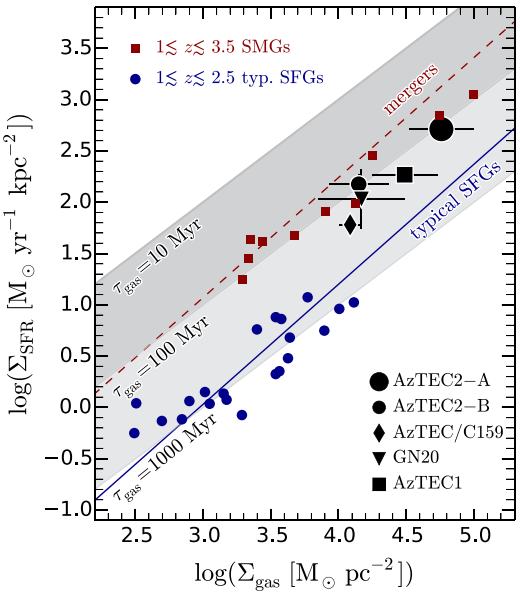

Figure 6. AzTEC2-A and AzTEC2-B in the Kennicutt–Schmidt ($\Sigma_{\rm SFR}$ – $\Sigma_{\rm gas}$) plane. For comparison, the massive, star-forming disks at $z \sim 4.5$ GN20 (Carilli et al. 2010; Hodge et al. 2012), AzTEC/C159 (Jones et al. 2017; Jiménez-Andrade et al. 2018), and AzTEC1 (Tadaki et al. 2018) are also shown, along with a compilation of typical SFGs over $1 \lesssim z \lesssim 2.5$ and SMGs over $1 \lesssim z \lesssim 3.5$ (Genzel et al. 2010, and references therein). In estimating $\Sigma_{\rm SFR}$ and $\Sigma_{\rm gas}$ of $z \sim 4.5$ star-forming disks we use their effective radius from dust-continuum emission and adopt $\alpha_{\rm CO} = 2.5\,M_{\odot}\,{\rm K^{-1}\,km^{-1}\,s\,pc^{-2}}$, except for AzTEC/C159, for which $\alpha_{\rm CO} = 4\,{\rm M_{\odot}\,K^{-1}\,km^{-1}\,s\,pc^{-2}}$ has been previously constrained. The horizontal error bars also take into account the $\Sigma_{\rm gas}$ range given by an $\alpha_{\rm CO}$ varying over 0.8–4.3 ${\rm M_{\odot}\,K^{-1}\,km^{-1}\,s\,pc^{-2}}$. The solid blue (dashed red) line illustrates the KS relation for typical SFGs (mergers) over the redshift range $1 \lesssim z \lesssim 3$ derived by Genzel et al. (2010). The gray diagonal lines show the $\Sigma_{\rm SFR}$ required to consume the available gas reservoirs within a gas depletion timescale ($\tau_{\rm gas}$) of 10 Myr (upper), 100 Myr (middle), and 1000 Myr (lower). The gray shaded regions illustrate the $\tau_{\rm gas}$ range for galaxies with (from top-to-bottom) high-to-low SFE.

merger-driven and massive star-forming disks that sustain vigorous star formation activity leading to SMG-like IR luminosities (e.g., Hayward et al. 2012).

5.2. The Cold Gas Accretion and Merger Mode of Star Formation at $z > 3$

The evidence of rotation-dominated, gas-rich, star-forming disks at $z > 4$ (e.g., Carilli et al. 2010; Hodge et al. 2012; De Breuck et al. 2014; Jones et al. 2017; Tadaki et al. 2018) indicates that high-redshift SMGs are not only merging, strongly perturbed systems (Tacconi et al. 2008; Engel et al. 2010; Younger et al. 2010; Riechers et al. 2011; Menéndez-Delmestre et al. 2014; Chen 2015; Jones et al. 2017; Chang et al. 2018). High-resolution (0.″07) dust-continuum imaging with ALMA has even shown evidence for spiral arms, bars, and rings in $z \gtrsim 2$ SMGs (Hodge et al. 2019). The remaining question is what are the mechanisms leading to the intense production of stars in such massive, star-forming disks in the early universe. We thus infer the locus of AzTEC2-A (and AzTEC2-B) in the Kennicutt–Schmidt plane (Figure 6) and use them as an observational diagnostic for constraining the global conditions for star formation in these systems.

We use the spatial extent of the dust-continuum emission from our ALMA observations (see Section 4.2) to infer the galaxy-averaged SFR surface density: $\Sigma_{\rm SFR} \equiv {\rm SFR}/(2\pi R_{\rm eff}^2)$. The effective radius containing half of the total emission, $R_{\rm eff}$, is approximated as $R_{\rm eff} \sim {\rm FWHM}/2.430$ (Murphy et al. 2017), assuming an exponentially declining surface brightness distribution as observed in disk galaxies. In order to approximate the galaxy-averaged molecular gas surface density ($\Sigma_{\rm gas} \equiv M_{\rm gas}/(2\pi R_{\rm eff}^2)$), we use our $M_{\rm gas}$ estimate based on $L'_{\rm CO(1\rightarrow0)}$ (Section 4.3) and $\alpha_{\rm CO} = 2.5\,M_{\odot}\,{\rm K^{-1}\,km^{-1}\,s\,pc^{-2}}$. Although the rotation-dominated gas disk of AzTEC2-A favors a higher $\alpha_{\rm CO}$ value (e.g., Papadopoulos et al. 2012a, 2012b; Jiménez-Andrade et al. 2018), we require more robust constraints (e.g., dynamical mass, metallicity, excitation conditions) to validate this scenario. We thus consider the uncertainties of $\Sigma_{\rm gas}$ associated with the unknown $\alpha_{\rm CO}$ value by illustrating in Figure 6 the $\Sigma_{\rm gas}$ range given by $\alpha_{\rm CO}$ varying from 0.8 to $4.3\,M_{\odot}\,{\rm K^{-1}\,km^{-1}\,s\,pc^{-2}}$. We also recall that in deriving $L'_{\rm CO(1\rightarrow0)}$, and hence $M_{\rm gas}$, we have assumed typical SMG-like gas excitation conditions, as previously observed in other massive, highly star-forming rotating disks like GN20 and AzTEC/C159 (Carilli et al. 2010; Hodge et al. 2012; Jiménez-Andrade et al. 2018). By combining our $\Sigma_{\rm gas}$ and $\Sigma_{\rm SFR}$ estimates we find that AzTEC2-A lies at the upper end of the Kennicutt–Schmidt relation for typical SFGs (Figure 6 Genzel et al. 2010). This is consistent with the properties of the massive, star-forming disks GN20 (Carilli et al. 2010; Hodge et al. 2012) and AzTEC/C159 (Jones et al. 2017; Jiménez-Andrade et al. 2018) at similar redshift. These systems arise as scaled (more active) versions of star-forming disks at lower redshifts ($1 \lesssim z \lesssim 2.5$ e.g., Daddi et al. 2010a, 2010b; Genzel et al. 2010, and references therein). Qualitatively, this is in agreement with the systematically higher gas fractions (e.g., Genzel et al. 2015; Schinnerer et al. 2016; Tacconi et al. 2018; Liu et al. 2019) and enhanced specific SFR of galaxies with increasing redshift (e.g., Karim et al. 2011; Speagle et al. 2014; Lehnert et al. 2015; Schreiber et al. 2015).

Figure 6 also suggests that massive, star-forming disks like AzTEC2-A, GN20, and AzTEC/C159 seem to harbor a systematically lower gas depletion timescale than their analogs at lower redshifts; which is compatible with the redshift evolution of $\tau_{\rm gas}$ of massive MS galaxies (e.g., Saintonge et al. 2013; Schinnerer et al. 2016; Tacconi et al. 2018; Liu et al. 2019). Such an efficient regime of star formation, that approaches that of merger-driven starbursts (Figure 6) could be explained by the turbulent ISM and rapid dynamical evolution that characterize high-redshift disks (e.g., Förster Schreiber et al. 2009; Bournaud et al. 2012; Swinbank et al. 2012). In this context, the enhanced stellar birth rate of early star-forming disks is a result of their inherent large gas reservoirs and –to some extent–a higher star formation efficiency ($\equiv 1/\tau_{\rm gas}$). Numerical simulations predict that at $z > 4$ the enhanced gas accretion from the cosmic web can maintain a gravitationally unstable gas-rich disk, which breaks into giant clumps and forms stars at a high rate (Bouché et al. 2007; Hodge et al. 2012; Romano-Díaz et al. 2014). Additionally, star formation in AzTEC2-A might be further enhanced due to gravitational interaction (torques) with its (minor) companion galaxy, AzTEC2-B, during the ongoing pre-coalescence phase—as inferred from hydrodynamic merger simulations (e.g., Cox et al. 2008; Moreno et al. 2015) and observations of galaxy pairs (Scudder et al. 2012). Although evidence of such tidal interactions could be inferred from an asymmetric (perturbed) velocity field of the gas (e.g., Kronberger et al. 2007), the incomplete coverage of the [C II]

velocity field of AzTEC2-A prevents us from confirming this scenario.

6. Summary

We have used multi-wavelength spectroscopic and photometric data to constrain the redshift and conditions for star formation in AzTEC2: the second brightest SMG (at 1.1 and 2 mm) in the COSMOS field. Our results are listed below:

1. AzTEC2 splits into two components (AzTEC2-A and AzTEC2-B) for which we detect ^{12}CO(5 → 4) and [C II] line emission, leading to a redshift of 4.626 ± 0.001 and 4.633 ± 0.001 for AzTEC2-A and AzTEC2-B, respectively;
2. The emission of AzTEC2-A and AzTEC2-B is mildly magnified by a foreground, massive elliptical galaxy at $z = 0.34$ located at ∼4″ to the south of AzTEC2-A,B. We estimate a magnification factor of $\mu_A = 1.5$ and $\mu_B = 1.35$ for AzTEC2-A and AzTEC2-B, respectively;
3. Based on the ^{12}CO(5 → 4) line emission of AzTEC2-A we have derived $\mu_A\, L'_{CO(1\rightarrow0)} = (12.8 \pm 2.4) \times 10^{10}$ K km s^{-1} pc^2, implying a molecular gas mass of $\mu_A M_{gas} = (1.0\text{–}5.5) \times 10^{11}\, M_\odot$. The FIR luminosity of AzTEC2-A leads to μ_A SFR $= (2880 \pm 140) M_\odot$ yr^{-1}, $L_{IR}/L'_{CO(1\rightarrow0)}$ ratio of $220 \pm 50\, L_\odot$(K km s^{-1} pc^2)$^{-1}$, and $\tau_{gas} = (35\text{–}190)$Myr;
4. Correspondingly, for AzTEC2-B we have found that $\mu_B\, L'_{CO(1\rightarrow0)} = (3.1 \pm 0.7) \times 10^{10}$ K km s^{-1} pc^2, $\mu_B\, M_{gas} = (0.25\text{–}1.3) \times 10^{11}\, M_\odot$, μ_B SFR $= 960 \pm 45\, M_\odot$ yr^{-1}, $L_{IR}/L'_{CO(1\rightarrow0)} = 310 \pm 80\, L_\odot$(K km s^{-1} pc^2)$^{-1}$, and $\tau_{gas} = (25\text{–}140)$Myr;
5. We have revealed a rotation-dominated [C II] disk in AzTEC2-A, with an intrinsic (deprojected) rotational velocity of $v_{rot}(i = 39°) = 660 \pm 130$ km s^{-1}, velocity dispersion of $\sigma \lesssim 100$ km s^{-1} and dynamical mass of $M_{dyn}(i = 39°) = 2.6^{+1.2}_{-0.9} \times 10^{11}\, M_\odot$.

Our results indicate that AzTEC2-A hosts a massive, rotation-dominated disk where star formation occurs at intense levels. This indicates that even disk galaxies that harbor vast gas reservoirs could sustain intense star formation activity that resembles that of merger-driven SMGs. This supports the emerging consensus whereby the population of single-dish-selected SMGs is rather heterogeneous, including both interacting systems and galaxies that form stars through a smoother mode of star formation sustained by cold gas accretion. A more systematic study of high-redshift star-forming disks is required to verify this scenario, allowing us to probe their properties within the framework of the cold and merger mode of star formation in the early universe.

We thank the reviewer for their careful reading of the manuscript and their constructive comments. We thank Justin Spilker for assistance with the gravitational lens modeling. E.F. J.A., B.M., E.R.D., A.K., K.C.H., and F.B. acknowledge support of the Collaborative Research Center 956, subproject A1 and C4, funded by the Deutsche Forschungsgemeinschaft (DFG). C.M.C. thanks the National Science Foundation for support through grants AST-1714528 and AST-1814034, and acknowledges support from the Research Corporation for Science Advancement from a 2019 Cottrell Scholar Award sponsored by IF/THEN, an initiative of Lyda Hill Philanthropies. C.M.C. and J.A.Z. also thank the University of Texas at Austin College of Natural Sciences for support. D.L. acknowledges support and funding from the European Research Council (ERC) under the European Union's Horizon 2020 research and innovation program (grant agreement No. 694343). I.A. acknowledges support from the CONACyT projects FDC-2016-1828 and CB-2016-281948. A.M. acknowledges support from the CONACyT project A1-S-45680. This paper makes use of the following ALMA data: ADS/JAO.ALMA 2015.1.00568.S. ALMA is a partnership of ESO (representing its member states), NSF (USA), and NINS (Japan), together with NRC (Canada), *MOST* and ASIAA (Taiwan), and KASI (Republic of Korea), in cooperation with the Republic of Chile. The Joint ALMA Observatory is operated by ESO, AUI/NRAO, and NAOJ. This work is based on observations carried out under project number W18EU with the IRAM NOEMA Interferometer. IRAM is supported by INSU/CNRS (France), MPG (Germany), and IGN (Spain). The National Radio Astronomy Observatory is a facility of the National Science Foundation operated under cooperative agreement by Associated Universities, Inc.

Facilities: Atacama Large Millimeter Array (ALMA), NOrthern Extended Millimeter Array (NOEMA).

ORCID iDs

E. F. Jiménez-Andrade https://orcid.org/0000-0002-2640-5917
J. A. Zavala https://orcid.org/0000-0002-7051-1100
B. Magnelli https://orcid.org/0000-0002-6777-6490
C. M. Casey https://orcid.org/0000-0002-0930-6466
D. Liu https://orcid.org/0000-0001-9773-7479
E. Romano-Díaz https://orcid.org/0000-0002-0071-3217
E. Schinnerer https://orcid.org/0000-0002-3933-7677
K. Harrington https://orcid.org/0000-0001-5429-5762
I. Aretxaga https://orcid.org/0000-0002-6590-3994
A. Karim https://orcid.org/0000-0002-8414-9579
J. Staguhn https://orcid.org/0000-0002-8437-0433
A. Montaña https://orcid.org/0000-0003-4229-381X
M. Yun https://orcid.org/0000-0001-7095-7543
F. Bertoldi https://orcid.org/0000-0002-1707-1775

References

Aravena, M., Spilker, J. S., Bethermin, M., et al. 2016, MNRAS, 457, 4406
Aretxaga, I., Wilson, G. W., Aguilar, E., et al. 2011, MNRAS, 415, 3831
Auger, M. W., Treu, T., Bolton, A. S., et al. 2009, ApJ, 705, 1099
Barger, A. J., Wang, W.-H., Cowie, L. L., et al. 2012, ApJ, 761, 89
Blain, A. W., Smail, I., Ivison, R. J., Kneib, J.-P., & Frayer, D. T. 2002, PhR, 369, 111
Bothwell, M. S., Aguirre, J. E., Chapman, S. C., et al. 2013, ApJ, 779, 67
Bothwell, M. S., Chapman, S. C., Tacconi, L., et al. 2010, MNRAS, 405, 219
Bothwell, M. S., Smail, I., Chapman, S. C., et al. 2013, MNRAS, 429, 3047
Bouché, N., Cresci, G., Davies, R., et al. 2007, ApJ, 671, 303
Bouché, N., Murphy, M. T., Kacprzak, G. G., et al. 2013, Sci, 341, 50
Bournaud, F., & Elmegreen, B. G. 2009, ApJL, 694, L158
Bournaud, F., Juneau, S., Floc'h, E. L., et al. 2012, ApJ, 757, 81
Brisbin, D., Miettinen, O., Aravena, M., et al. 2017, A&A, 608, A15
Bruzual, G., & Charlot, S. 2003, MNRAS, 344, 1000
Calderón-Castillo, P., Nagar, N. M., Yi, S., et al. 2019, A&A, arXiv:1904.09300
Cañameras, R., Yang, C., Nesvadba, N. P. H., et al. 2018, A&A, 620, A61
Carilli, C. L., Daddi, E., Riechers, D., et al. 2010, ApJ, 714, 1407
Carilli, C. L., & Walter, F. 2013, ARA&A, 51, 105
Casey, C. M., Chen, C.-C., Cowie, L. L., et al. 2013, MNRAS, 436, 1919

Casey, C. M., Cooray, A., Killi, M., et al. 2017, ApJ, 840, 101
Casey, C. M., Narayanan, D., & Cooray, A. 2014, PhR, 541, 45
Chang, Y.-Y., Ferraro, N., Wang, W.-H., et al. 2018, ApJ, 865, 103
Chen, C.-C. & ALESS, ALMA-S2CLSconsortia 2015, ASP Conf. Ser. 499 in Revolution in Astronomy with ALMA: the Third Year, ed. D. Iono (San Francisco, CA: ASP), 13
Courteau, S. 1997, AJ, 114, 2402
Cox, T. J., Jonsson, P., Somerville, R. S., Primack, J. R., & Dekel, A. 2008, MNRAS, 384, 386
da Cunha, E., Groves, B., Walter, F., et al. 2013, ApJ, 766, 13
Daddi, E., Bournaud, F., Walter, F., et al. 2010a, ApJ, 713, 686
Daddi, E., Dannerbauer, H., Liu, D., et al. 2015, A&A, 577, A46
Daddi, E., Elbaz, D., Walter, F., et al. 2010b, ApJL, 714, L118
Davé, R., Finlator, K., Oppenheimer, B. D., et al. 2010, MNRAS, 404, 1355
Davies, R., Schreiber, N. M. F., Cresci, G., et al. 2011, ApJ, 741, 69
De Breuck, C., Williams, R. J., Swinbank, M., et al. 2014, A&A, 565, A59
Dekel, A., Birnboim, Y., Engel, G., et al. 2009a, Natur, 457, 451
Dekel, A., Sari, R., & Ceverino, D. 2009b, ApJ, 703, 785
Delhaize, J., Smolčić, V., Delvecchio, I., et al. 2017, A&A, 602, A4
Di Teodoro, E. M., Fraternali, F., & Miller, S. H. 2016, A&A, 594, A77
Downes, D., & Solomon, P. M. 1998, ApJ, 507, 615
Draine, B. T., & Li, A. 2007, ApJ, 657, 810
Drew, P. M., Casey, C. M., Burnham, A. D., et al. 2018, ApJ, 869, 58
Elbaz, D., Leiton, R., Nagar, N., et al. 2018, A&A, 616, A110
Ellison, S. L., Mendel, J. T., Scudder, J. M., Patton, D. R., & Palmer, M. J. D. 2013, MNRAS, 430, 3128
Engel, H., Tacconi, L. J., Davies, R. I., et al. 2010, ApJ, 724, 233
Erickson, N., Narayanan, G., Goeller, R., & Grosslein, R. 2007, ASP Conf. Ser. 375 in From Z-Machines to ALMA: (Sub)Millimeter Spectroscopy of Galaxies, ed. A. J. Baker (San Francisco, CA: ASP), 71
Förster Schreiber, N. M., Genzel, R., Bouché, N., et al. 2009, ApJ, 706, 1364
Fudamoto, Y., Ivison, R. J., Oteo, I., et al. 2017, MNRAS, 472, 2028
Gao, Y., & Solomon, P. M. 2004, ApJ, 606, 271
Geach, J. E., Dunlop, J. S., Halpern, M., et al. 2017, MNRAS, 465, 1789
Geach, J. E., Narayanan, D., Matsuda, Y., et al. 2016, ApJ, 832, 37
Geach, J. E., Smail, I., Moran, S. M., et al. 2011, ApJL, 730, L19
Genzel, R., Tacconi, L. J., Gracia-Carpio, J., et al. 2010, MNRAS, 407, 2091
Genzel, R., Tacconi, L. J., Lutz, D., et al. 2015, ApJ, 800, 20
Gobat, R., Strazzullo, V., Daddi, E., et al. 2012, ApJL, 759, L44
Gómez-Guijarro, C., Toft, S., Karim, A., et al. 2018, ApJ, 856, 121
Hammer, F., Flores, H., Puech, M., et al. 2009, A&A, 507, 1313
Harrington, K. C., Yun, M. S., Magnelli, B., et al. 2018, MNRAS, 474, 3866
Hayward, C. C., Bremer, M. N., Chen, C.-C., et al. 2018, MNRAS, 476, 2278
Hayward, C. C., Jonsson, P., Kereš, D., et al. 2012, MNRAS, 424, 951
Hayward, C. C., Kereš, D., Jonsson, P., et al. 2011, ApJ, 743, 159
Hayward, C. C., Primack, J. R., Moreno, J., et al. 2013, MNRAS, 434, 2572
Helou, G., Soifer, B. T., & Rowan-Robinson, M. 1985, ApJL, 298, L7
Hodge, J. A., Carilli, C. L., Walter, F., et al. 2012, ApJ, 760, 11
Hodge, J. A., Smail, I., Walter, F., et al. 2019, ApJ, 876, 130
Hodge, J. A., Swinbank, A. M., Simpson, J. M., et al. 2016, ApJ, 833, 103
Hopkins, P. F., Cox, T. J., Younger, J. D., & Hernquist, L. 2009, ApJ, 691, 1168
Hung, C.-L., Hayward, C. C., Smith, H. A., et al. 2016, ApJ, 816, 99
Ikarashi, S., Ivison, R. J., Caputi, K. I., et al. 2015, ApJ, 810, 133
Iono, D., Yun, M. S., Aretxaga, I., et al. 2016, ApJL, 829, L10
Ivison, R. J., Smail, I., Amblard, A., et al. 2012, MNRAS, 425, 1320
Jiménez-Andrade, E. F., Magnelli, B., Karim, A., et al. 2018, A&A, 615, A25
Jiménez-Andrade, E. F., Magnelli, B., Karim, A., et al. 2019, A&A, 625, A114
Jin, S., Daddi, E., Liu, D., et al. 2018, ApJ, 864, 56
Jones, G. C., Carilli, C. L., Shao, Y., et al. 2017, ApJ, 850, 180
Karim, A., Schinnerer, E., Martínez-Sansigre, A., et al. 2011, ApJ, 730, 61
Katz, H., Kimm, T., Sijacki, D., & Haehnelt, M. G. 2017, MNRAS, 468, 4831
Kennicutt, J. R. C. 1998, ARA&A, 36, 189
Kereš, D., Katz, N., Weinberg, D. H., & Davé, R. 2005, MNRAS, 363, 2
Kohandel, M., Pallottini, A., Ferrara, A., et al. 2019, MNRAS, 487, 3007
Kronberger, T., Kapferer, W., Schindler, S., & Ziegler, B. L. 2007, A&A, 473, 761
Lagache, G., Cousin, M., & Chatzikos, M. 2018, A&A, 609, A130
Laigle, C., McCracken, H. J., Ilbert, O., et al. 2016, ApJS, 224, 24
Lang, P., Schinnerer, E., Smail, I., et al. 2019, ApJ, 879, 54
Le Fèvre, O., Béthermin, M., Faisst, A., et al. 2019, A&A, submitted, arXiv:1910.09517
Le Floc'h, E., Aussel, H., Ilbert, O., et al. 2009, ApJ, 703, 222
Lehnert, M. D., van Driel, W., Le Tiran, L., Di Matteo, P., & Haywood, M. 2015, A&A, 577, A112
Leroy, A. K., Bolatto, A., Gordon, K., et al. 2011, ApJ, 737, 12
Liu, D., Daddi, E., Dickinson, M., et al. 2018, ApJ, 853, 172
Liu, D., Gao, Y., Isaak, K., et al. 2015, ApJL, 810, L14
Liu, D., Schinnerer, E., Groves, B., et al. 2019, ApJ, 887, 235
LúHillier, B., Combes, F., & Semelin, B. 2012, A&A, 544, A68
Lutz, D., Poglitsch, A., Altieri, B., et al. 2011, A&A, 532, A90
Magnelli, B., Ivison, R. J., Lutz, D., et al. 2015, A&A, 573, A45
Magnelli, B., Karim, A., Staguhn, J., et al. 2019, ApJ, 877, 45
Magnelli, B., Lutz, D., Saintonge, A., et al. 2014, A&A, 561, A86
Magnelli, B., Saintonge, A., Lutz, D., et al. 2012, A&A, 548, A22
Maiolino, R., Caselli, P., Nagao, T., et al. 2009, A&A, 500, L1
Menéndez-Delmestre, K., Blain, A. W., Swinbank, M., et al. 2014, RMxAC, 44, 85
Miettinen, O., Delvecchio, I., Smolčić, V., et al. 2017, A&A, 597, A5
Miettinen, O., Smolčić, V., Novak, M., et al. 2015, A&A, 577, A29
Miller, S. H., Bundy, K., Sullivan, M., Ellis, R. S., & Treu, T. 2011, ApJ, 741, 115
Moreno, J., Torrey, P., Ellison, S. L., et al. 2015, MNRAS, 448, 1107
Mullaney, J. R., Alexander, D. M., Goulding, A. D., & Hickox, R. C. 2011, MNRAS, 414, 1082
Murphy, E. J., Momjian, E., Condon, J. J., et al. 2017, ApJ, 839, 35
Narayanan, D., Hayward, C. C., Cox, T. J., et al. 2010, MNRAS, 401, 1613
Narayanan, D., Turk, M., Feldmann, R., et al. 2015, Natur, 525, 496
Newman, S. F., Genzel, R., Förster-Schreiber, N. M., et al. 2012, ApJ, 761, 43
Oliver, S. J., Bock, J., Altieri, B., et al. 2012, MNRAS, 424, 1614
Papadopoulos, P. P., van der Werf, P., Xilouris, E., Isaak, K. G., & Gao, Y. 2012a, ApJ, 751, 10
Papadopoulos, P. P., van der Werf, P. P., Xilouris, E. M., et al. 2012b, MNRAS, 426, 2601
Persic, M., Salucci, P., & Stel, F. 1996, MNRAS, 281, 27
Riechers, D. A., Capak, P. L., Carilli, C. L., et al. 2010, ApJL, 720, L131
Riechers, D. A., Carilli, C. L., Capak, P. L., et al. 2014, ApJ, 796, 84
Riechers, D. A., Hodge, J., Walter, F., Carilli, C. L., & Bertoldi, F. 2011, ApJL, 739, L31
Robertson, B. E., & Bullock, J. S. 2008, ApJL, 685, L27
Rodighiero, G., Daddi, E., Baronchelli, I., et al. 2011, ApJL, 739, L40
Romano-Díaz, E., Shlosman, I., Choi, J.-H., & Sadoun, R. 2014, ApJL, 790, L32
Rybak, M., Rivera, G. C., Hodge, J. A., et al. 2019, ApJ, 876, 112
Saintonge, A., Lutz, D., Genzel, R., et al. 2013, ApJ, 778, 2
Sanders, D. B., & Mirabel, I. F. 1996, ARA&A, 34, 749
Schinnerer, E., Carilli, C. L., Capak, P., et al. 2008, ApJL, 689, L5
Schinnerer, E., Groves, B., Sargent, M. T., et al. 2016, ApJ, 833, 112
Schinnerer, E., Sargent, M. T., Bondi, M., et al. 2010, ApJS, 188, 384
Schreiber, C., Pannella, M., Elbaz, D., et al. 2015, A&A, 575, A74
Scott, K. S., Austermann, J.E., Perera, T.A., et al. 2008, MNRAS, 385, 2225
Scudder, J. M., Ellison, S. L., Torrey, P., Patton, D. R., & Mendel, J. T. 2012, MNRAS, 426, 549
Shao, Y., Wang, R., Jones, G. C., et al. 2017, ApJ, 845, 138
Smolčić, V., Aravena, M., Navarrete, F., et al. 2012, A&A, 548, A4
Smolčić, V., Karim, A., Miettinen, O., et al. 2015, A&A, 576, A127
Smolčić, V., Miettinen, O., Tomičić, N., et al. 2017, A&A, 597, A4
Smolčić, V., Novak, M., Bondi, M., et al. 2017, A&A, 602, A1
Solomon, P. M., Downes, D., Radford, S. J. E., & Barrett, J. W. 1997, ApJ, 478, 144
Speagle, J. S., Steinhardt, C. L., Capak, P. L., & Silverman, J. D. 2014, ApJS, 214, 15
Spilker, J. S., Marrone, D. P., Aravena, M., et al. 2016, ApJ, 826, 112
Springel, V., & Hernquist, L. 2005, ApJL, 622, L9
Stott, J. P., Swinbank, A. M., Smail, I., et al. 2016, MNRAS, 457, 1888
Swinbank, A. M., Sobral, D., Smail, I., et al. 2012, MNRAS, 426, 935
Tacchella, S., Dekel, A., Carollo, C. M., et al. 2016, MNRAS, 457, 2790
Tacconi, L. J., Genzel, R., Saintonge, A., et al. 2018, ApJ, 853, 179
Tacconi, L. J., Genzel, R., Smail, I., et al. 2008, ApJ, 680, 246
Tacconi, L. J., Neri, R., Chapman, S. C., et al. 2006, ApJ, 640, 228
Tadaki, K., Iono, D., Yun, M. S., et al. 2018, Natur, 560, 613
Toft, S., Gallazzi, A., Zirm, A., et al. 2012, ApJ, 754, 3
Toft, S., Smolčić, V., Magnelli, B., et al. 2014, ApJ, 782, 68
Toft, S., Zabl, J., Richard, J., et al. 2017, Natur, 546, 510
Willick, J. A. 1999, ApJ, 516, 47
Wuyts, S., Schreiber, N. M. F., van der Wel, A., et al. 2011, ApJ, 742, 96
Yang, C., Omont, A., Beelen, A., et al. 2017, A&A, 608, A144
Younger, J. D., Fazio, G. G., Ashby, M. L. N., et al. 2010, MNRAS, 407, 1268
Yun, M. S., Aretxaga, I., Gurwell, M.A., et al. 2015, MNRAS, 454, 3485
Zavala, J. A., Montaña, A., Hughes, D. H., et al. 2018, NatAs, 2, 56
Zavala, J. A., Yun, M.S., Aretxaga, I., et al. 2015, MNRAS, 452, 1140